Space Weather

RESEARCH ARTICLE
10.1029/2022SW003305

Statistical Temporal Variations in the Auroral Electrojet Estimated With Ground Magnetometers in Fennoscandia

Simon Walker[1], Karl Laundal[1], Jone Reistad[1], Anders Ohma[1], and Spencer Hatch[1]

[1]Department of Physics and Technology, Birkeland Centre for Space Science, University of Bergen, Bergen, Norway

Key Points:

- A new inversion technique for Spherical Elementary Current analysis is implemented and tested
- A new data set based on a fixed set of ground magnetometers in Fennoscadia is presented
- We identify when and where temporal variations in the radial magnetic field are strongest

Correspondence to:

S. Walker,
simon.walker@uib.no

Citation:

Walker, S., Laundal, K., Reistad, J., Ohma, A., & Hatch, S. (2023). Statistical temporal variations in the auroral electrojet estimated with ground magnetometers in Fennoscandia. *Space Weather*, *21*, e2022SW003305. https://doi.org/10.1029/2022SW003305

Received 29 SEP 2022
Accepted 7 JAN 2023

Author Contributions:

Conceptualization: Simon Walker, Karl Laundal
Data curation: Simon Walker
Formal analysis: Simon Walker
Funding acquisition: Karl Laundal
Methodology: Simon Walker
Project Administration: Karl Laundal
Software: Simon Walker
Supervision: Karl Laundal, Jone Reistad
Validation: Simon Walker
Visualization: Simon Walker
Writing – original draft: Simon Walker
Writing – review & editing: Simon Walker, Karl Laundal, Jone Reistad, Anders Ohma, Spencer Hatch

Abstract We present the implementation of an improved technique to coherently model the high-latitude ionospheric equivalent current. Using a fixed selection of 20 ground magnetometers in Fennoscandia, we present a method based on Spherical Elementary Current Systems (SECS) to model the currents coherently during 2000–2020. Due to the north-south extent of the magnetometers, we focus on the model output along the 105° magnetic meridian. Our improvements involve fixed data locations and SECS analysis grid and using a priori knowledge of the large-scale currents improving the robustness of the inverse problem solution. We account for contributions from ground induced currents assuming so-called mirror currents. This study produces a new data set of divergence-free (DF) currents and magnetic field perturbations along the 105° magnetic meridian with 1-min resolution. By comparing averages of the data set with an empirical model of the ionosphere we demonstrate the validity of the data set. We show how our data set, in particular its temporal nature, is distinct from empirical models and other studies. Not only can the temporal evolution of the DF currents and magnetic field perturbations be investigated, but the time derivative of said quantities can be analyzed. For application in ground induced currents, we present the statistical properties of where (in magnetic latitude and local time) and at what rate ($\partial B_r/\partial t$) the radial magnetic field component fluctuates, a temporal derivative that has received very little attention. We show that $\partial B_r/\partial t$ is dependent on latitude, local time, and solar cycle. We present other applications such as Ultra Low Frequency Waves monitoring.

Plain Language Summary A number of Sun driven processes that can lead to phenomena such as the northern and southern lights, generate electric currents within the ionosphere, an ionized part of the atmosphere. We use a fixed set of ground magnetic field measurements in Fennoscandia to robustly map these currents. Taking advantage of the regularity of the measurements, we not only produce a 20 year time series of the currents and magnetic field but also present statistics of the temporal change of disturbances in the radial magnetic field. This derivative is an important property in understanding the impacts of space weather on modern infrastructure, in particular it can cause large current spikes that disrupt power grids over a relatively large area.

1. Introduction

The link between the Sun and geomagnetic field disturbances has been reported for a long time. In 1852 Sabine identified a link between the number of sunspots, which is an indicator of solar activity, and geomagnetic field disturbances. He found that during a minimum in the sunspot number we experience a reduction in geomagnetic field disturbances (Cliver & Cliver, 1994). Historical reports have shown that for centuries large scale features on the photosphere have coincided with observations of significant, intense geomagnetic activity in the form of low latitude aurora (Schove, 1983), however the mechanisms behind this were not understood. With the arrival of work by Chapman and Birkeland in the late 19th and early 20th century, the description of the Earth's magnetosphere immersed within the solar wind came into focus. Birkeland's early work introduced a current system, which bears his name, flowing in and out of the polar ionosphere. Despite his initial theories involving a stream of high velocity electrons being emitted from the Sun, he moved to the realization of a neutral solar wind made up of both electrons and positively charged ions (Birkeland, 1908; Chapman & Ferraro, 1931). Although a different current system and theory outlined by Chapman prevailed for some time, with the arrival of space based magnetometers Birkeland's theory proved fruitful as it explained the magnetic field perturbations observed (Zmuda et al., 1966). Chapman and Ferraro's work transformed the field of space physics when they described how magnetic storms are manifested through introduction of the magnetosphere and how it interacts with the solar wind (Chapman & Ferraro, 1931; Siscoe, 2001).

In more modern times we know that the solar wind is a quasi-neutral supersonic plasma streaming out of the Sun dragging with it the Sun's magnetic field, due to the frozen-in effect, into interplanetary space. How this interplanetary magnetic field (IMF) couples with the Earth's magnetic field holds particular importance for the dynamics of the polar ionosphere and magnetosphere. This can be described by the Dungey cycle. The Dungey cycle is a generalized, simplified, steady-state description of how, during periods of a southward oriented IMF, dayside geomagnetic flux is opened and reconnected with the IMF before being dragged over the polar cap, subsequently stimulating preexisting open flux in the magnetotail to reconnect. This newly closed flux then convects to the dayside magnetosphere (Dungey, 1961). In the region of the ionosphere, plasma flows are driven by the motion of magnetic flux around the ionosphere. At certain altitudes these plasma flows create a current system due to collisions between ions and neutrals causing a differential motion between the ions and electrons. Currents along the dawn and dusk flanks are referred to as the westward and eastward electrojets respectively. Ground magnetometers have been historically used to study the strength and extent of these electrojets. Such measurements are not affected by the magnetic field of the field aligned Birkeland currents and their associated connecting currents, a realization made by Fukushima and thus has been named Fukushima's theorem. Fukushima's theorem states that under the approximation of a radial magnetic field (which is most valid in the polar regions), the magnetic signature of curl-free (CF) currents, whose source and sink are the Birkeland currents, cancel below the current layer (Fukushima, 1976). Conversely, the magnetic signature of the divergence-free (DF) currents are observable above and below the current layer. Fukushima's theorem shows us why we needed space based magnetometers for Birkeland's theories to be confirmed (Fukushima, 1994; Zmuda et al., 1966). Harang utilized ground based magnetometers to identify a discontinuity between the westward and eastward electrojets (Harang, 1946; Koskinen & Pulkkinen, 1995). This discontinuity commonly coincides with the location of substorm onsets (Weygand et al., 2008), consequently relating the electrojets to the closure of magnetotail flux described in the Dungey cycle.

There is an abundance of ground based magnetometers providing good coverage of measurements of the auroral electrojets, particularly in regions such as North America and Fennoscandia. Spherical harmonic analysis has been a core part of modeling DF ionospheric currents using ground based magnetometers. More recent techniques still have the methodology of Chapman and Bartels (1940) at their core (Laundal et al., 2016, 2018). However, the meaning of the spherical harmonic model output in regions where magnetometer coverage is sparse is often unclear and difficult to interpret. Amm (1997) introduced a technique called spherical elementary current systems which focuses on modeling limited regions. This approach models the DF and CF components of the ionospheric currents on a 2D spherical shell independently using two different spherical elementary currents systems (SECS). Amm and Viljanen (1999) derived the magnetic field from the current a SECS produces. Therefore, we can recreate the magnetic field measured on ground using a weighted sum of DF SECS and consequently find a current that produces those magnetic field perturbations.

In previous studies DF SECS has proven to have a vast array of applications. Weygand et al. (2012) used DF SECS and ground magnetometers to produce estimates of the DF currents and compare them with measurements of convection with SuperDARN. During the summer they show that the DF currents can be used to predict the ionospheric convection, without the necessity of conditions for backscatter that limits the SuperDARN data set. In another study, the SECS amplitudes are compared with measurements of the region 1 and 2 currents using magnetometers on board the DMSP satellites (Weygand & Wing, 2016) and a significant resemblance is found. Many studies of the DF currents have focused on magnetospheric and ionospheric dynamics due to solar wind driving conditions and addressed questions of substorm onset phenomena (Vanhamäki & Juusola, 2020; Weygand et al., 2011, 2021). By placing SECS at both the ionospheric current layer and at a certain depth within the ground, the SECS method has been useful for separating observed magnetic perturbations into telluric and ionospheric sources (Juusola et al., 2020; Pulkkinen, Amm, Viljanen, et al., 2003).

In this study we build upon the DF SECS method and incorporate a new SECS inversion technique introduced by Laundal et al. (2021) for use with data from the Electrojet Zeeman Imaging Explorer (EZIE) mission, which will be launched in 2024. EZIE will be capable of making remote measurements of the magnetic field using the Zeeman effect (Yee et al., 2021). The inversion technique, used by Laundal et al. (2021), involves a priori information about the structure of the electrojet. Here we apply this technique to 20 ground magnetometers in Fennoscandia that were simultaneously available at 1-min resolution for a total of approximately 11 years between 2000 and 2020. The technique produces 2D maps of the electrojet and associated magnetic field, but we focus on an output along a 1D slice along the 105° magnetic meridian, in quasi-dipole co-ordinates, which is particularly

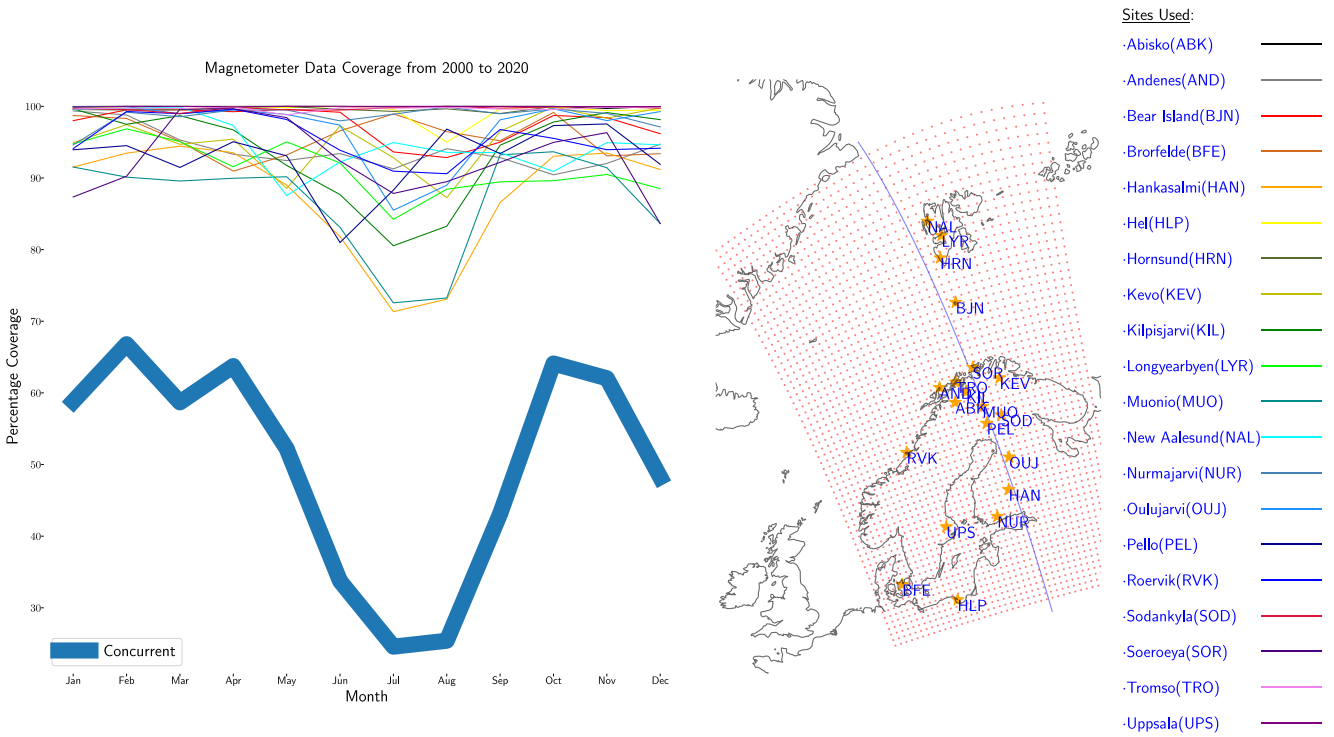

Figure 1. (Left panel) Monthly data coverage of each chosen magnetometer and their availability concurrently. (Right panel) Spherical Elementary Current Systems pole locations as red dots, orange stars to show the location of the magnetometers used in this study and a green line that is the 105° magnetic meridian that the model is evaluated along.

well covered by the magnetometers. The resulting data set, which is publicly available (Walker et al., 2022b), consists of ground magnetic field perturbations and ionospheric sheet current densities along this meridian. We also highlight the interpretation of the time derivative of the radial magnetic field dB_r/dt as the radial component of the curl of the geomagnetically induced electric field (GIE) (Vanhamäki et al., 2013) and present a statistical analysis of the properties of this quantity. This analysis stands in contrast to the analysis of the time derivative of the horizontal magnetic field (often denoted $\partial\mathbf{H}/\partial t$), which has received comparatively much more attention (Dimmock et al., 2020; Juusola et al., 2020; Rogers et al., 2020; Schillings et al., 2022; Tanskanen et al., 2001; Viljanen et al., 2001; Weigel et al., 2003).

In Sections 2 and 3, we respectively present the data and our application of SECS to derive the DF currents. In Section 4 we demonstrate the validity of the approach by comparing the large scale statistics of the DF current and associated radial magnetic field structure with those of an empirical model (Laundal et al., 2018). We also present our statistical analysis of $\partial B_r/\partial t$. In Section 5 we discuss our findings, and in Section 6 we conclude the paper.

2. Data

We use data with 1-min time resolution from 20 magnetometers in Fennoscandia obtained through the SuperMAG collaboration (Gjerloev, 2012), see Figure 1. SuperMAG has its own method of subtracting the baseline of the magnetic field from the magnetometer measurements. As outlined in Gjerloev (2012), there are three core components of the calculated baseline: the diurnal variations, the yearly trend and the remaining residual during quiet periods. The diurnal variations aim to include contributions from the solar quiet (Sq) currents and variations with a local time dependence, such as temperature effects on the instruments. The yearly trend primarily consists of the Earth's time dependent magnetic field. The residual component is determined by the remaining magnetic field during official magnetic quiet periods. It is unlikely that baseline methodology is able to remove all the influences listed, in particular those that vary on shorter time scales, such as the Sq currents, however considering the high latitude of observations we can be confident that their magnetic signature is small in comparison to that of the electrojets.

The SuperMAG data is provided in local magnetic co-ordinates, in which the northward component points along the quiet-day horizontal component of the main magnetic field. This study uses the geodetic co-ordinate system and as such the data needs to be rotated into this system. To rotate the horizontal magnetic field, a declination angle between the local magnetic north and geodetic north is required. We choose to use the CHAOS-7 core and crustal magnetic field model (Finlay et al., 2020) to find the declination angle at each station and rotate the vectors into the geodetic system.

To reduce ambiguity as to what causes variations in the modeled DF currents, we require that all the magnetometers that are chosen for the SECS inversion are available at the same time. Figure 1 shows how often our 20 magnetometers are available individually and simultaneously (thick blue line). This combination of stations has been chosen to maximize the total coverage of simultaneous measurements, approximately 11 years over a period from 2000 to 2020. We find a dip in coverage during the summer months in a number of magnetometers that impacts the overall concurrent coverage. We are also aware that there is little concurrent data in 2015 due to a drop in the availability of data from Hankasalmi and Muonio. Figure 1 also shows the grid that we use in our analysis (discussed in Section 3), and the 105° magnetic meridian, where we evaluate the currents and magnetic field components. We see from the figure that this meridian passes through a high density of magnetometers.

3. Method

In this study we apply a recently developed Spherical Elementary Current System (SECS) inversion technique to ground magnetometers. SECS analysis represents ionospheric and telluric currents as the weighted sum of multiple small-scale currents. The weights are determined from magnetometer measurements. It can thus be used as a way to interpolate magnetic fields and currents from a set of individual non-uniformly distributed magnetometers to a continuous map. Here we give a brief overview of the SECS analysis technique, describe our methodology and highlight how this methodology addresses problems within previous work.

Magnetic fields on ground can be modeled as 2D horizontal DF currents that flow on spherical shells above and/or below the Earth's surface (Chapman & Bartels, 1940). Such modeling has historically been accomplished using spherical harmonic analysis. Amm (1997) presented DF basis functions that are more suitable for regional analyses, which he called SECS. The SECS basis functions are global but with a short reach. Placed sufficiently dense, and scaled appropriately, they can be used to represent any well-behaved 2D vector field on a sphere (Vanhamäki & Juusola, 2020). With these basis functions, a DF surface current density $\vec{J}$ at a radius R can be written as

$$\vec{J}(\vec{r}) = \sum_i \frac{I_i \hat{\vec{e}}_{\phi_i}}{4\pi R} \cot\left(\frac{\theta_i}{2}\right) \tag{1}$$

where $\vec{r}$ is the position where $\vec{J}$ is evaluated. The sum is over a set of DF SECS with amplitudes I_i. θ_i is the angular distance from the SECS to $\vec{r}$, and $\hat{\vec{e}}_{\phi_i}$ is an eastward unit vector in a coordinate system where the SECS is at the pole. In Equation 1 R could be above ground (above R_E, radius of the Earth), for modeling ionospheric currents, or below ground, for modeling telluric currents.

The magnetic field of one single DF SECS was calculated by Amm and Viljanen (1999) through the Biot-Savart law. The analytic expressions for the θ (southward), ϕ (eastward), and r (radial) magnetic fields, in a local system centered on the SECS pole, are:

$$\Delta B_{\theta_i}(\theta_i, r) = \frac{-\mu_0 I_i}{4\pi r \sin\theta_i} \begin{cases} \dfrac{s - \cos\theta_i}{\sqrt{1 + s^2 - 2s\cos\theta_i}} + \cos\theta_i & r < R \\ \dfrac{1 - s\cos\theta_i}{\sqrt{1 + s^2 - 2s\cos\theta_i}} - 1 & r > R \end{cases} \tag{2}$$

$$\Delta B_{\phi_i}(\theta_i, r) = 0 \tag{3}$$

$$\Delta B_r(\theta_i, r) = \frac{\mu_0 I_i}{4\pi r}\begin{cases} \dfrac{1}{\sqrt{1+s^2-2s\cos\theta_i}} - 1 & r < R \\ \dfrac{s}{\sqrt{1+s^2-2s\,cos\,\theta_i}} - s & r > R \end{cases} \tag{4}$$

$$s = \min(r, R)/\max(r, R). \tag{5}$$

In our case, we use magnetometers on ground, so $r = R_E$. However, we model currents both in the ionosphere ($R = R_I > R_E$) and below ground ($R = R_T < R_E$), so both versions of the equations are needed. These expressions are for a single elementary system, and the total magnetic field at $\vec{r}$ is the sum over all. This gives a linear relationship between magnetic field measurements and SECS amplitudes:

$$G\vec{m} = \vec{d}, \tag{6}$$

where $\vec{m}$ is a vector that contains the SECS amplitudes, $\vec{d}$ is a vector that contains all 60 magnetic field components from the 20 magnetometers, and G is a matrix that relates $\vec{m}$ and $\vec{d}$ according to the equations above. We return shortly to how we solve this system of equations for $\vec{m}$.

The grid of SECS can be as dense or as sparse as desired. Although a more dense grid of systems can capture finer structure, two points must be considered: (a) whether the measurements can resolve so fine a structure (for magnetometers one must take into account the spacing of the magnetometers and the smoothing of the magnetic signal with increasing distance from the source (Laundal et al., 2021)); (b) a denser grid requires more model parameters, therefore solving for these parameters becomes more computationally expensive. Furthermore, a number of previous studies have placed the elementary systems in a regular grid in longitude and latitude Vanhamäki and Juusola (2020), Juusola et al. (2006, 2016, 2020). This leads to a more dense grid in physical space at increasing latitudes. We choose to place our elementary current systems above and below the ground in a grid that is regular in cubed sphere coordinates (Ronchi et al., 1996; Sadourny, 1972). The cubed sphere grid is regular in physical space and does not have the same problem. The grid is displayed in the right panel in Figure 1, in a Lambert Conformal projection. The grid has been chosen with an average spacing of 50 km, positioned so that the magnetometers are not within 10 km of a SECS pole and oriented toward approximately magnetic north in magnetic Quasi-Dipole (QD) coordinates (Richmond, 1995), using an epoch of 2008. Furthermore, the radial placement of the elementary systems is an important consideration, as we model the ionospheric and telluric currents as two shells of sheet currents, we must pick an altitude and depth that can mimic the magnetic field created from the 3 dimensional ionospheric and telluric current systems. In total we have $N = 2{,}814$ grid cells, with $2N$ elementary currents, one set above the ground at 110 km altitude, and one set below the ground, where the chosen depth is introduced later in this section. However, a fixed depth for the telluric currents is either more problematic due to the variability in the 3 dimensional ground conductance and the variability in the temporal scales of variations in the ionospheric inducing current which results in the induction peaking at varying depths.

We clearly have many more elementary current systems than data points, which means that the inverse problem of finding the SECS amplitudes from a small set of measurements is severely under-determined. This can be partly rectified by using a simplifying assumption about how the ionospheric currents are related to their induced counterpart in the ground. We choose that the radial magnetic field perturbations from the ionospheric and telluric currents exactly cancel at a 500 km depth (the telluric poles are placed at a depth derived from Equation A5 in Juusola et al. (2016) that depends on the altitude of the ionospheric poles and the cancellation depth). Then, as detailed by Juusola et al. (2016), the mirror current magnitudes are precisely determined by the ionospheric current magnitudes, reducing the number of unknowns from $2N$ to N. This method ascribes the term "image currents" to the currents modeled by the telluric SECS poles. This name comes from the assumption that the telluric currents will mirror the ionospheric currents.

Even with this simplification, the problem remains under-determined; there are an infinite number of SECS amplitude combinations that will fit the observations within some fixed precision. In this section we address the criteria in which we choose the solution to the inverse problem. Most recent studies that use SECS analysis (Amm, 1997; Pulkkinen, Amm, & Viljanen, 2003; Pulkkinen, Amm, Viljanen, et al., 2003; Vanhamäki & Juusola, 2020; Weygand et al., 2021) handle this problem by using truncated singular value decomposition

(TSVD). By zeroing singular values below a certain cutoff, the spatial structure of the DF current is encouraged to be less complex. However, this approach implements very little prior knowledge of DF currents. In contrast, in this study we implement Tikhonov regularization, similar to a recent study by Laundal et al. (2021), who presented a technique for SECS analysis for mesospheric magnetic field data from the upcoming EZIE satellite mission. Using regularization we aim to encourage electrojet like structures, which exhibit small current gradients in the magnetic east-ward direction, and, much like TSVD, encourage reduced current complexity, something we expect due to the distance of the measurements from the source and the need for multiple magnetometers to measure the structure to resolve it. Following Laundal et al. (2021)'s approach, we find the set of SECS amplitudes, $\vec{m}$, that minimizes:

$$f = \|G\vec{m} - \vec{d}\|^2 + \lambda_1 \|I\vec{m}\|^2 + \lambda_2 \|L_e\vec{m}\|^2, \tag{7}$$

where I is the $N \times N$ identity matrix, and L_e is an $N \times N$ matrix that, when multiplied by $\vec{m}$, yields the gradient of the SECS amplitudes in the QD eastward direction. The first term in Equation 7 is the sum of squared errors. If we only minimized this term, $\vec{m}$ would be the least squares solution. The second term represents the squared length of the model vector, multiplied by the parameter λ_1. Increasing λ_1 will limit the overall magnitude of the components in the solution vector, effectively decreasing the spatial complexity of the solution. Increasing λ_1 has a similar effect as increasing the cutoff value in a TSVD inversion. The third term in Equation 7 describes the sum of the squared magnitudes of the magnetic eastward gradients in the SECS amplitude, scaled by λ_2. Increasing λ_2 limits the eastward gradients. The rationale for including this term is that ionospheric electrodynamics tends to be structured east-west (Harang, 1946).

Since the location of our magnetometers and SECS poles are fixed, we choose a constant set of values for λ_1 and λ_2. If λ_1 is too much larger than λ_2 the amplitudes no longer have a smooth gradient in the magnetic east-west direction. If λ_2 is too much larger than λ_1 the amplitudes become thin bands in the east-west direction because there is no restriction in the variation in the north-south direction. Furthermore, even if the λ values are well balanced, if both are too large the model will not represent the data because the first term (the data-model misfit) will not be significant enough. With these things in mind, and after inspecting a great number of cases, we chose $\lambda_1 = 10^{-23}$ and $\lambda_2 = 10^{-21}$. These numbers are based on the use of SI units. Since the magnetometer locations, SECS locations, and regularization parameters are all fixed, our inversion results are directly comparable across the whole data set.

3.1. Examples

Figures 2 and 3 show two examples where the technique described above was applied. The left panels show the magnetic field on the ground, where the background color represents the modeled radial magnetic field perturbations, and black the arrows represent the modeled horizontal component. The orange stars show the locations of the magnetometers. The red arrows represent the measured horizontal magnetic field and the colored dot in the center of the star the radial component. The second panels from the left shows the SECS pole amplitudes in color. In the third panels, the arrows represent the modeled ionospheric currents and the color its magnitude. The final panel shows a slice of the ionospheric currents along the 105° magnetic meridian, which is particularly well covered by data. The publicly available data set, Walker et al. (2022b), includes the ground magnetic field and equivalent current along this meridian, with spacing ≈70 km.

With Equation 1, the DF current can be calculated at, in principle, any location. However, very close to a SECS pole, the magnitude approaches infinity. Therefore, we follow Vanhamäki and Juusola (2020) and introduce a correction (see their Equation 2.44) closer than 50 km from the SECS poles. This correction is only applied when evaluating the DF current, and not to the magnetic field, which is not as severely affected by the singularity due to the distance between the currents and the ground.

Figure 2 is based on 1 min of data taken at 22:34 UT on the 5th of February 2000. By looking at the left panel, we see that the model and the measurements are in good agreement. The second panel clearly shows that the SECS amplitudes have small gradients in the east-west direction and shows large areas of similar amplitude. This is a clear case of a strong east-west electrojet. Figure 3 shows another example, based on 1 min of magnetometer data at 20:25 UT on the same day. Again, the model and the measurements are in good agreement. Here, on the other hand, we see a strong northward current. This shows that the λ values in Equation 7 are not so large as to prevent north-south structures when the data indicates that such structures exist.

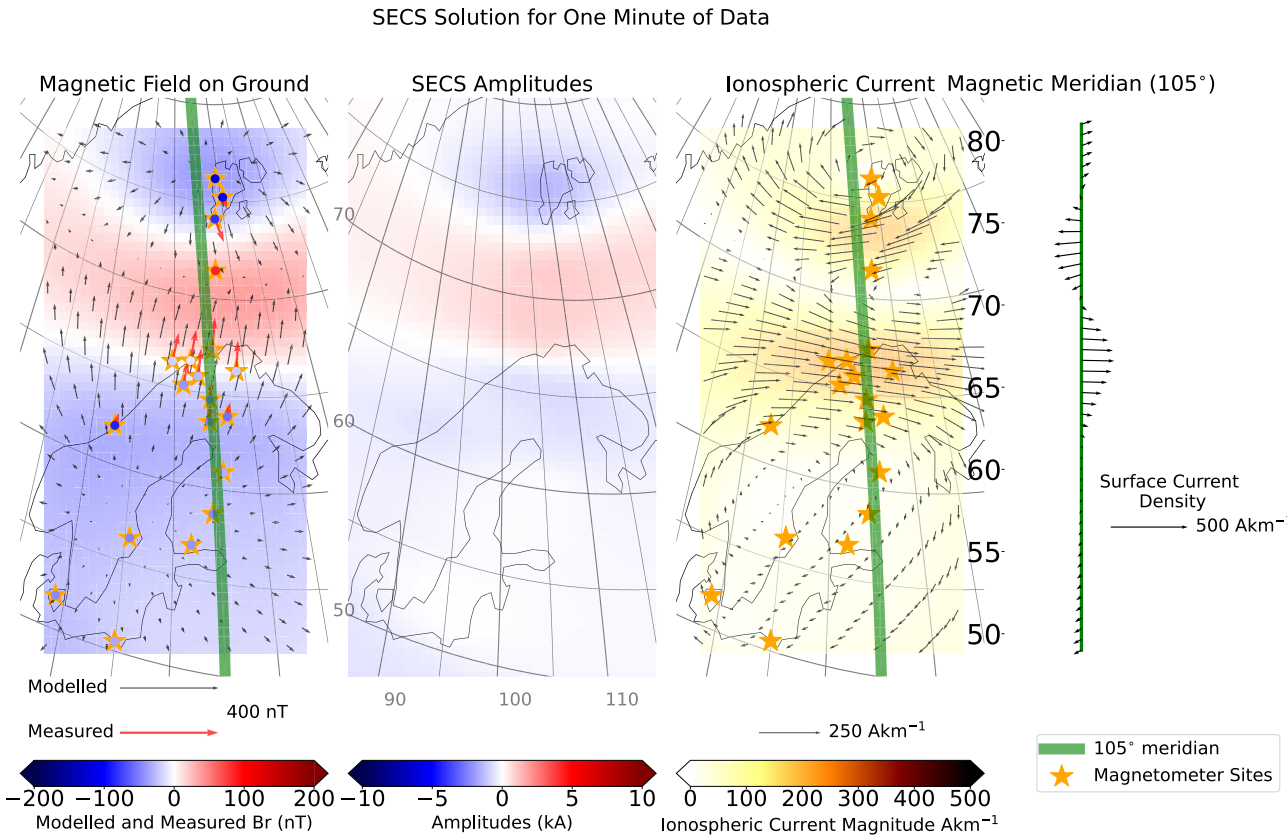

Figure 2. The figure shows the application of the methodology described in Section 3 where the currents and magnetic field are estimated by fitting Spherical Elementary Current Systems (SECS) amplitudes using magnetic field measurements. The left panel shows the estimated horizontal magnetic field as black arrows, the estimated radial magnetic field as the background color, the location of the magnetometers as orange stars, the measured horizontal magnetic field as red arrows and measured radial magnetic as colored dot in the center of the stars. The second panel from the left shows the SECS pole amplitudes as the background color. The third panel from the left shows the estimated divergence-free currents as black arrows and the magnitude of the currents with the background color. The third panel from the left also shows the location of the magnetometers as orange stars. The right panel shows the estimated divergence-free currents along the 105° magnetic meridian, at different magnetic latitudes, as black arrows. The location and extent of the 105° magnetic meridian, where the model is evaluated for every minute of data, is shown as a green line in the first panel and third panel from left. The time in UTC of the magnetometer data used for this inversion is 22:34 05/02/2000.

With the methodology tested through the use of case studies, we apply it to every instance where SuperMAG provides data from all 20 magnetometers. At each instance we calculate an independent set of model amplitudes and use them to estimate the DF currents in the ionosphere and the ground magnetic field along the 105° magnetic meridian. The resulting data set is N_t independent instances of currents and magnetic fields at 50 points, evenly spaced, between 49° and 81° mlat, where N_t is the total number of minutes where data from all 20 magnetometers has been provided.

4. Results

We now present results based on our data set, minute-cadence magnetic field perturbations and associated eastward and northward sheet current density along the 105° QD meridian. First we compare the currents and radial magnetic field from an empirical model to a large-scale average based on our data set. This comparison is used as validation. The data set's relatively high time resolution enables investigation of spatiotemporal structures in a way that is not possible with empirical large-scale, average models. We therefore subsequently present an analysis of the temporal changes in the radial magnetic field ($\partial B_r/\partial t$).

4.1. Large-Scale Average Current Structure

Here we compare a large-scale average current and radial magnetic field pattern to predictions from the Average Magnetic field and Polar current System (AMPS) model. The AMPS model (Laundal & Toresen, 2018; Laundal

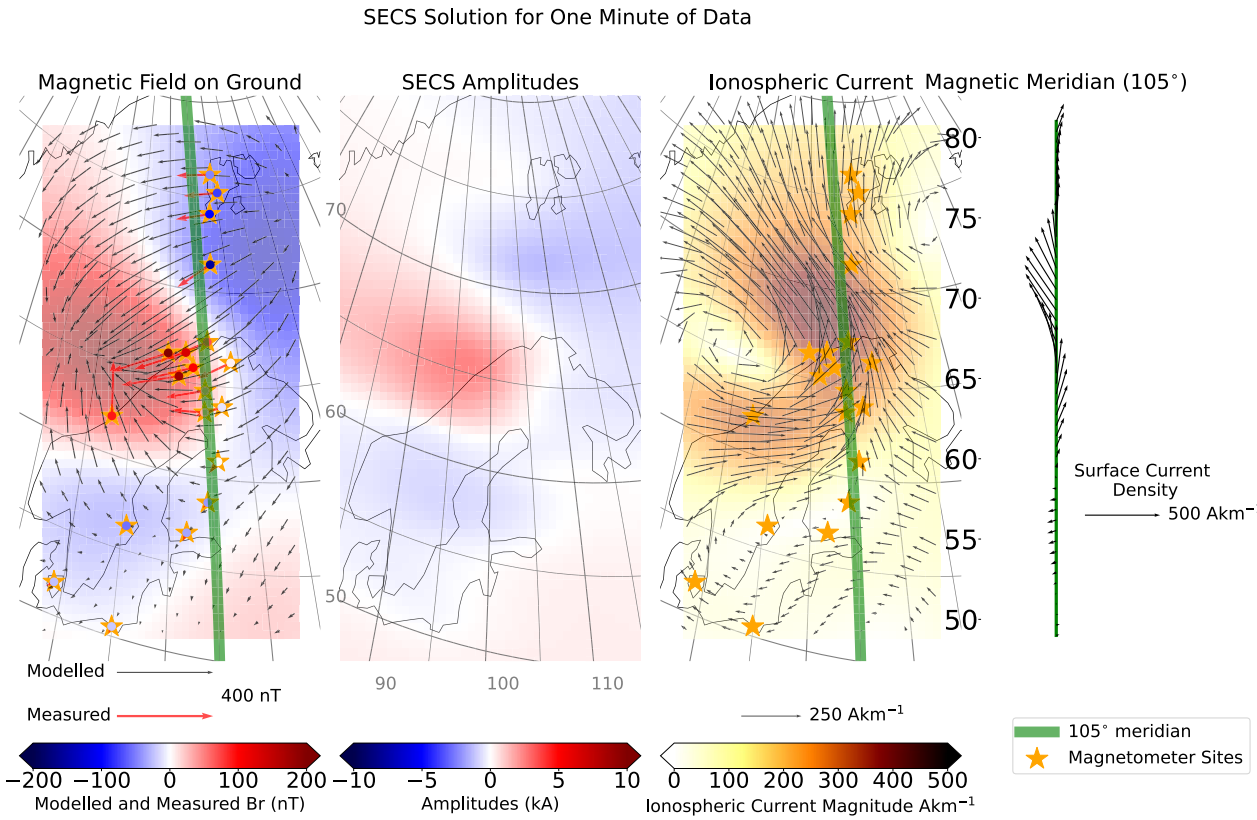

Figure 3. This figure uses the same set up as Figure 2. The time in UTC of the magnetometer data used for this inversion is 20:25 05/02/2000.

et al., 2018) is an empirical model of the ionospheric magnetic field and current system generated using magnetic field measurements from *Swarm* and the Challenging Minisatellite Payload (CHAMP) satellites. AMPS takes user inputs of solar F10.7 cm flux, solar wind speed, IMF B_y and B_z, and the Earth's dipole tilt.

To compare our data set to AMPS prediction it is important to make a selection of our data set that is restrictive enough for the average to be a good general description of the range of data within that selection, while having enough data to produce a reliable average. We have tested a variety of selections but for the purpose of paper we present three clock angles, −135°, 180°, and 135°. For each angle we select instances when the IMF clock angle is within a 45° wide window centered at that clock angle. To reduce the effects of extreme events and produce the typical electrodynamics expected from the Dungey cycle (i.e., the two cell convection pattern) we select our electrojet and radial magnetic field estimates when they occur during the following conditions: IMF B_y is between −10 and 10 nT, IMF B_z is between 0 and −10 nT, and the dipole tilt angle is less than 0°. Further measures are taken to ensure that the data selected is under the influence of these conditions by using a similar approach to Haaland et al. (2007): We apply a 30-min rolling average to OMNI data (King & Papitashvili, 2005), that is time shifted to the bow shock, and associate it with our data set by having the average made up of OMNI data 20 min prior and 10 min after the SECS meridian was evaluated. Furthermore, we calculate the circular variance of IMF B_y and B_z in the same windows as a measure of how stable the conditions are. We then add a further selection criteria that the circular variance associated with our data set must be less than 0.04.

Figure 4 (top row) shows the average horizontal sheet current and radial magnetic field based on this data selection, on a grid of magnetic latitude and local time. A corresponding AMPS prediction is shown on the bottom row, using the median conditions of the solar wind, IMF, solar flux and dipole tilt of the times selected to make the SECS based map. Figure 4 shows that the general shape of the radial magnetic field perturbations and electrojet are similar in the two approaches. This demonstrates that the technique produces results that are consistent with expectations from earlier studies. However, in Figure 4 there are some notable differences between the two plots particularly in terms of the magnitude of the currents and the radial magnetic field. We also see a difference in the shape and location of the cells of the radial magnetic field that are most prominent at higher latitudes. One

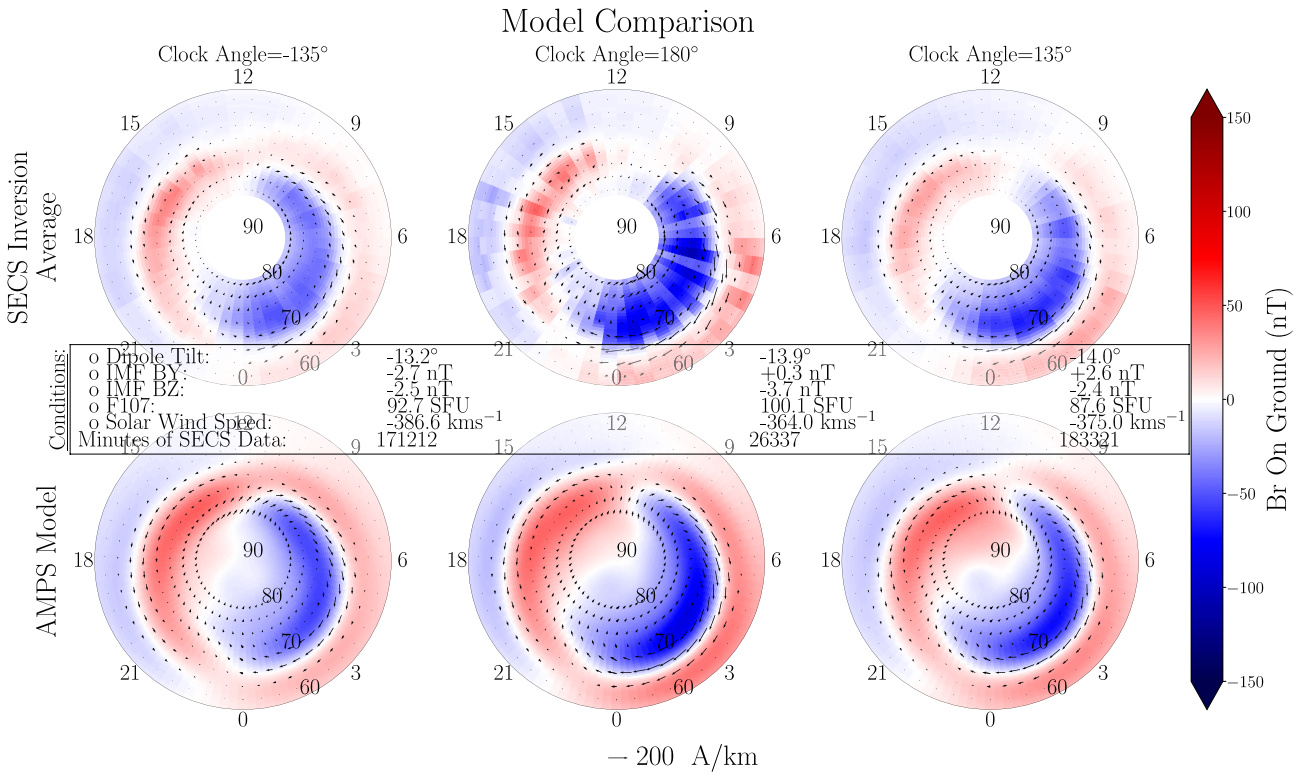

Figure 4. The figure shows three plots containing an average of each instance of the Spherical Elementary Current Systems (SECS) model output along the 105° meridian, that occur under different criteria, and three plots with a corresponding output from the Average Magnetic field and Polar current System (AMPS) model. The top row shows a polar view of the average divergence-free sheet current density in the ionosphere and radial magnetic field perturbations on the ground, modeled along the 105° meridian for each minute of simultaneous measurements from all 20 magnetometers, occurring under the range of conditions specified in Section 4.1 and have a clock angle that is within a window centered at −135°, 180°, and 135° respectively and with a width of 45°. The bottom row shows a polar view of the divergence-free sheet current density and radial magnetic field output from the AMPS model when run with each set of the conditions specified in the conditions box, which are the median conditions for the selected instances of each of the SECS model outputs.

difference between the two approaches is that the AMPS current by definition is DF, while our average current pattern in general is not. Our technique enforces DF currents at any given time, but averages composed of several meridians do not have this constraint. We reiterate that the main advantage of our approach over average models is that it allows analyses of spatio-temporal variations. We explore this further in the rest of this section.

4.2. Occurrence Rate of Large Magnetic Field Variations

Temporal variations in the radial component of the magnetic field ($\partial B_r/\partial t$) are equivalent to the radial component of the curl of the purely induced (DF) electric field, otherwise known as the GIE (Vanhamäki et al., 2013). The large amount of data (11 years' worth of 1-min data, spanning 20 years), and the consistency in the technique makes our data set ideal for analyzing how GIEs in Fennoscandia vary in relation to other parameters. This is also important for space weather applications, since variations in the magnetic field cause ground induced currents (GICs), which have negative consequences for human infrastructure, such as the electrical power grid (Albertson et al., 1993; Molinski, 2002; Oliveira & Ngwira, 2017).

Figure 5 shows the likelihood of observing temporal variations of the radial magnetic field perturbations (or equivalently, the radial component of the curl of GIEs), the difference in the radial magnetic field between two instances along the 105° meridian separated by 1 min, above a certain magnitude for the entire data set produced but excluding instances with a gap greater than 1 min. The y axis shows the magnetic latitude, and the x axis shows the threshold for a positive detection. Negative x corresponds to decreases in B_r and positive x corresponds to increases. The color and contours show the number of occurrences divided by the number of observations. The occurrence is presented in a logarithmic style where $10^{-5.7}$ is an occurrence of once per year. The figure is approximately symmetrical suggesting that large increases and large decreases are just as common at similar latitudes. Two peaks, identified by red ellipses in Figure 5, stand out, the first occurs at approximately 67° latitude,

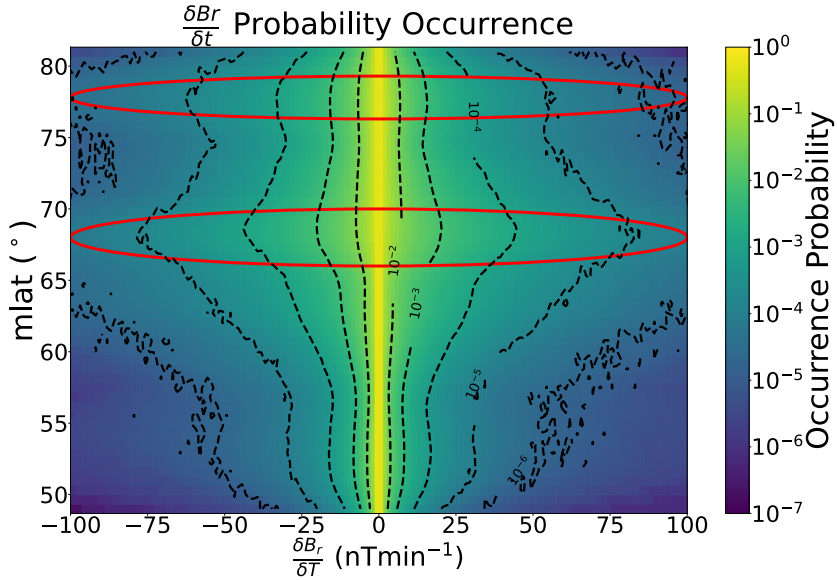

Figure 5. A plot of the statistics of fluctuations of the radial component of the magnetic field evaluated on the ground along the 105° mlon meridian. The contours and color are the cumulative probability of getting increases (decreases) in B_r that are at least the fluctuation indicated on the positive (negative) part of the x axis. Red ellipses highlight the two main peaks in the occurrence of a large derivative of B_r.

close to the northern most coast of Norway, and the second at approximately 77° latitude, close to Ny-Ålesund. The larger of the two is near the average latitude of substorm disturbances and the location of the electrojets. The smaller of the two may be related to high latitude return currents. Explanations for the double peak are explored further in Section 5.2.

Figure 6 shows the occurrence probability of large fluctuations as a function of magnetic local time and magnetic latitude for the entire data set produced but excluding instances with a gap greater than 1 min. We choose to regard fluctuations greater than 25 nT min^{-1} as large based on Figure 5. We see two peaks, the largest again at approximately 67° latitude, close to the northern coast of Norway, and the second at approximately 77° latitude, near to Ny–Ålesund. The strongest peak forms a smooth circle at similar latitudes for all MLTs, however, exhibiting higher occurrence probability in the pre-midnight sector. This is the typical location for substorm onsets (Frey et al., 2004). The high latitude peak is strongest in the pre-midnight and pre-noon regions. The pre-midnight high-latitude peak may also be associated with substorms. We discuss the occurrence probability distribution in greater detail in Section 5.2 and pay particular focus to the mechanisms that may be the cause of the pre-noon high latitude peak.

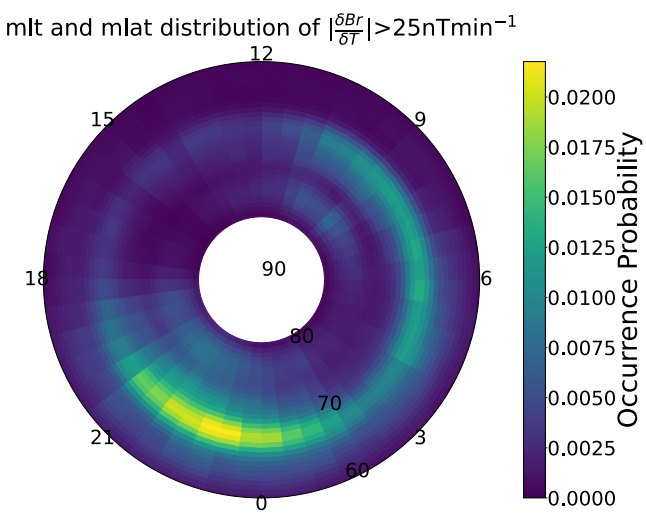

Figure 6. Figure showing the probability of a fluctuation of a radial magnetic field perturbation of magnitude greater than 25 nT/min. The figure is in mlt-mlat space where the color represents the occurrence probability.

Figure 7 shows how the probability of large fluctuations in the radial magnetic field perturbation varies over the solar cycle. The occurrence probability is calculated by finding the meridians that have $\delta B_r/\delta t$ greater than 25 nT/min at any latitude. The occurrence probability shows an approximate 3 year offset with the peak in sunspot number and peaks during the declining phase. This is the same behavior recorded in the solar wind velocity. This observation is in agreement with current literature where both wave phenomena and substorm occurrence statistics show a correlation with solar wind velocity (Dimmock et al., 2016; Hynönen et al., 2020; Newell et al., 2016; Nosé et al., 1995; Nykyri et al., 2017; Tanskanen et al., 2005).

5. Discussion

We have presented a technique to derive magnetic fields and equivalent currents along the 105° magnetic meridian, based on measurements from 20

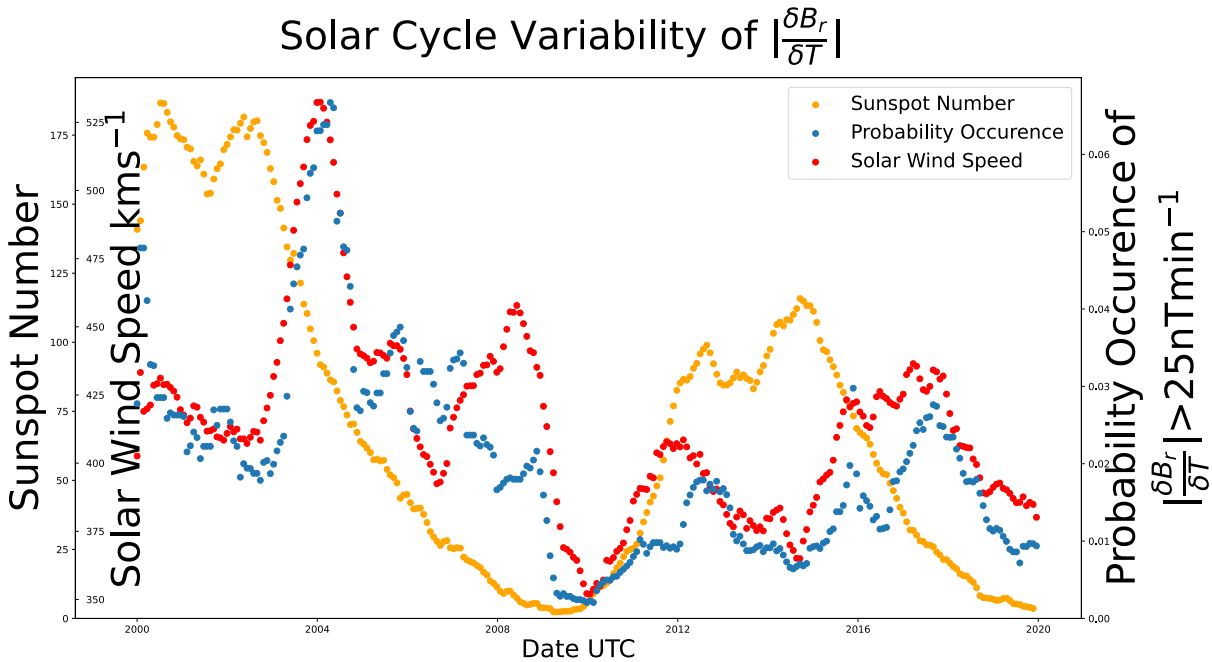

Figure 7. Figure showing the sunspot number, the solar wind speed, and the probability of observing fluctuations in B_r greater than 25 nT/min anywhere along the meridian. The quantities are first grouped into 27 days (one Carrington rotation), taking the mean, and then a 365 day window rolling mean is applied to remove relatively short time scale fluctuations.

magnetometers in Fennoscandia. Currents and magnetic field perturbations along this meridian are released in accompaniment with the paper (Walker et al., 2022b). The data set is not without limitations due to the decisions made in magnetometer choice, SECS grid choice and methodology. The temporal coverage of the magnetometers has a bias toward winter months and their spatial distribution impacts the scale size of currents that can be resolved, which we describe in Section 2 and discuss further in Section 5.4. The varying ground conductivity over the region, in particular between ground and sea water, can cause a bias in the magnetic field perturbations at a magnetometer and is another aspect of the impacts of choice of magnetometers. We discuss and explore impacts of this on the data set later in Section 5.2. As we discussed in Section 3, the ionospheric and telluric currents are simplified as two dimensional shells and the radial placement of these shells and the coverage of the grid limits its ability to create suitable current structures that are representative of the magnetic perturbations from the three dimensional DF currents. Different values for the regularization parameters, λ_1 and λ_2, that are chosen in Section 3 could yield different data set. Although repetition of the steps taken to reach said parameters, in particular by different users, may yield different values, the differences are likely small, if the criteria in Section 3 are met, and, therefore, will have little impact on the data set. Of course different regularization schemes, such as one in the temporal domain, will have implications on the data set produced and we return to the discussion of methodology development in further studies section, Section 5.4.

5.1. Relevance of the New Data Set and Technique

In this section we summarize the data set and the model introduced. We discuss the advantages of the approach used and the avenues of research where the data set can contribute.

A comparable study is Aakjær et al. (2016) that utilizes the magnetometers on board the European Space Agency's *Swarm* satellites. By using a similar approach to Olsen (1996), the auroral electrojet is modeled for each pass of a *Swarm* satellite by fitting a series of line currents orthogonal to the satellite track using the measured magnetic field magnitude. The use of satellites in Aakjær et al. (2016) has the advantage that they cover regions inaccessible to ground magnetometers. However, the *Swarm* satellites orbit above ≈450 km which means that their distance from the ionospheric current layer will limit the resolvable electrojet structure, compared to what can be achieved with a dense ground network. The constant location of measurements, the longevity of

magnetometer operation and constant high latitude observations enables a much larger data set bringing greater confidence to the statistics produced and the ability to tackle temporal phenomena.

Compared to previous SECS based analyses of ground-based magnetometer measurements (Marsal et al., 2017; Vanhamäki et al., 2003; Weygand & Wing, 2016; Weygand et al., 2011, 2012), the present study is distinct in a number of ways: We keep a constant selection of ground magnetometers and SECS poles, thus keeping a constant model geometry, which allows us to produce a consistent data set that spans 20 years. This enables the study of long-term temporal variations and structures in the magnetic field, as demonstrated in Section 4.1. Also our application of Tikhonov regularization to solve the SECS inverse problem, in particular the use of first order Tikhonov regularization, is different to the more commonly applied, TSVD since it implies knowledge of electrojet structure to encourage solutions that are aligned in the magnetic east-west direction unless the data indicates otherwise.

In this study we use the regularization approach introduced by Laundal et al. (2021) for the application to the EZIE satellites that are planned for launch in 2024. EZIE will remotely detect the magnetic field at ≈80 km altitude using the Zeeman effect (Yee et al., 2021). At this altitude the influence of telluric currents is negligible. The high density of measurements and their vicinity to the electrojet will allow EZIE to resolve fine structures in the electrojets. One application of EZIE, as a continuation of this and other studies, is to utilize two layers of measurements (EZIE and ground magnetometers) to improve the separation of magnetic fields from telluric and ionospheric currents. Combining EZIE measurements at 80 km altitude with both ground and low Earth orbit measurements of magnetic perturbations will allow for further investigation of large and small scale features with unprecedented 3D coverage.

There are many avenues to developing this technique further. First, the methodology by Juusola et al. (2020) can be used to improve upon the approach used to account for the influence of telluric currents, thus modeling the ionospheric currents more accurately. Second, much like Green et al. (2007) did with spherical cap harmonics, we can use a combination of ground and satellite measurements of the magnetic field to constrain a superposition of DF and CF SECS (Amm, 1997; Amm & Viljanen, 1999). This allows us to take advantage of a regional approach to estimate currents with finer structure than is achieved by the Active Magnetosphere and Planetary Response Experiment (AMPERE) (Anderson et al., 2014). Furthermore, we can now use shorter data windows than Green et al. (2007). We can then analyze the ionospheric currents at time scales closer to substorm dynamics. Unlike other studies (Laundal et al., 2022) we will estimate the ionospheric currents based only on the magnetic field data, without further knowledge of the ionospheric state.

5.2. $\partial B_r/\partial t$

Figures 5 and 6 show that there are two clear peaks in the probability of large temporal variations in B_r, one at auroral latitudes and one at higher latitudes. There are several possible explanations for the latitudinal distribution of the occurrence of large fluctuations in the radial magnetic field: The density of magnetometers is necessarily smaller in the ocean region between northern Norway and Svalbard, with a single magnetometer at Bjørnøya. This may increase the relative importance of the damping terms in our cost function (Equation 7), leading to a smaller B_r and thus smaller $\partial B_r/\partial t$. Another explanation is that the peak coincides with the peak in the latitudinal distribution of electrojets.

An alternative geological explanation for the double peak is that the difference between the high conducting sea water and less conductive ground around coastal magnetometers leads to an enhanced radial magnetic field from the induced currents, as discussed by Juusola et al. (2020). The method that we use to take into account ground-induced currents is incapable of accounting for this effect of varying conductivity. While this does not affect our estimates of the magnetic field it will affect our estimates of the DF ionospheric current. A repeat of this study on magnetometers in other regions may allow us to eliminate the effects of geography in the model by comparing the occurrence distributions from the different data sets. Improved techniques in accounting for the influence of telluric currents, such as that presented by Juusola et al. (2020), can be used in future research to perform a better separation of the ionospheric and telluric contributions to the magnetometer measurements. In any case, improving our model of the telluric currents is not likely to have any influence on the results shown in Figures 5–7 as we are fitting B_r, and either approach will be a similar interpolation of the measurements of the radial magnetic field perturbation.

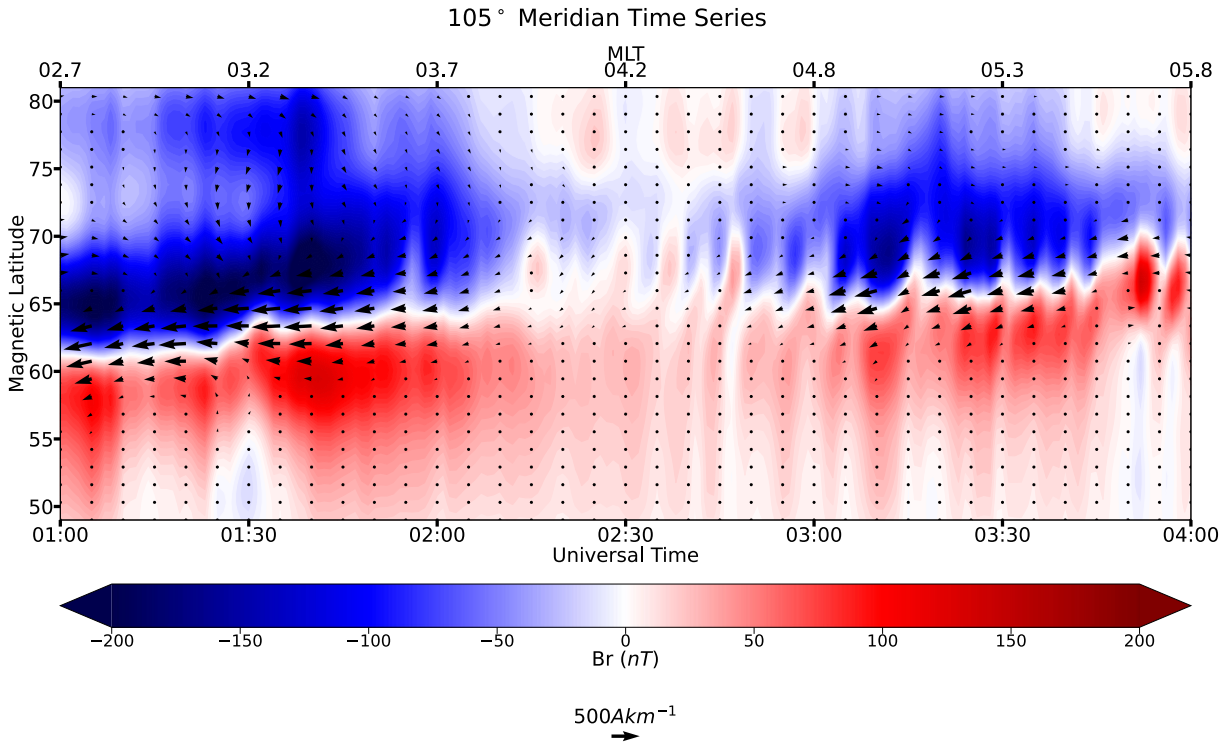

Figure 8. Time series of the data set with sheet current density vectors reduced to a cadence of 5 min and 25 data points along the meridian. The data is from the morning sector on the 28th of January 2000.

While the latitudinal distribution, in Figures 5 and 6, may be influenced by geological effects unique to our data set (i.e., the local effect of the coastline), the MLT distribution, in Figure 6, is less affected. Therefore the MLT distribution and latitudinal distribution, excluding the region between the Norwegian coast and Svalbard, can be interpreted in terms of ionospheric dynamics. Figure 6 shows that there is a peak in the occurrence of large $\partial B_r/\partial t$ at the common location of substorm onsets, 23 hr MLT, with a second peak at high latitudes at around 9 hr MLT. We also observe but have not presented that the time derivative of the horizontal magnetic field, as reported by Viljanen et al. (2001), evinces a similar MLT and MLAT distribution. In Figure 6 we also see a peak in the occurrence probability at high latitudes in the pre-noon sector. This peak may be associated with the current driven by a rapid solar wind pressure increase as described by Madelaire et al. (2022). This hypothesis can be addressed in future work by reproducing these statistics under common favorable conditions, such as a northward orientated IMF, to see if the features in the statistics become enhanced. Another theory is that the peak is related to a high occurrence of ULF waves. Conditions are known to be favorable for ULF waves in the solar wind on the dawn side of the magnetosphere (Plaschke et al., 2018). Nosé et al. (1995) identified a distribution in ULF waves, from the magnetometer on-board Dynamics Explorer 1, that also peaks pre-noon at a high latitude. Furthermore, Weigel et al. (2003) investigated the time derivative of the horizontal magnetic field and found the occurrence of strong $\delta H/\delta t$ at a similar location, attributing this peak to the influence of ULF waves. Section 5.3 shows that the SECS methodology implemented in this study does reproduce waves and can be used to investigate such phenomena. The hypothesis, in regards to the distribution of ULF waves, can be addressed in future work by analyzing the periodicity of these fluctuations and their contribution to the presented statistics.

5.3. ULF Wave Visualization

Figure 8 shows an example of the magnetic field and DF current at the 105° meridian as a function of time and MLT. The color shows the radial magnetic field on ground, including both ionospheric and internal contributions. The vectors show the equivalent current corresponding to the ionospheric contribution to the observed magnetic field. The figure was produced by stacking vertical latitudinal profiles horizontally. The lower x-axis shows the universal time, and the top x-axis shows the magnetic local time of the 105° meridian. This "magnetic

field keogram" shows how the electrojet can change over time and how the zero point of the radial magnetic field perturbations tracks the center of the electrojet.

Figure 8 shows clear evidence of ULF waves in periodic fluctuations of the radial magnetic field perturbations. This is most clearly seen between 2:10 and 3:00 universal time (UT). The figure illustrates that the 1-min resolution magnetic field model, evaluated along the 105° meridian allows easy visual identification of waves, and wave characteristics such as amplitude, phase and frequency. An investigation into the occurrence and magnitude of ULF waves could help test the hypothesis presented in Section 4.2, that the pre-noon high latitude peak may be explained by such phenomena.

5.4. Future Studies

The technique presented here is also applicable with other data sets. A number of magnetometers have higher cadence measurements than are used in this study. The IMAGE chain has a 10-s cadence for all their magnetometers, some even have 1-s cadence. Using these magnetometers, this study could be repeated and higher frequency waves in the magnetic field evaluated along the meridian could be resolved. Furthermore, we show that in Section 2 and Figure 1 that there is a seasonal bias in our data set due to the availability of some magnetometers selected, a selection of magnetometers could be made with the reduction of data availability bias in mind rather than to maximize the overall data, as was done in this study. Additionally, as stated previously, the methodology could be applied to different regions and the study repeated. For example, North America has great coverage on magnetometers; performing a similar study using those magnetometers could allow us to verify or refute the geological hypotheses surrounding the peaks in the latitudinal distribution of the occurrence of large $\partial B_r/\partial t$. The study can also be repeated for conjugate chains of magnetometers, such as those in Greenland and Antarctica, to investigate inter-hemispheric differences. Finally, the inversion methodology could have additional regularization parameters, where further expectations could be imposed on the electrojet structure, for example, a temporal regularization parameter could be used to imply a degree of smoothness in the evolution of the electrojet structure. However, in this case one must consider the impact on the validity of the derivative statistics investigated in this study.

6. Conclusions

We have presented a new technique for the application of DF SECS and applied it to 20 ground magnetometers in Fennoscandia. This has yielded a new data set of DF currents along the 105° magnetic meridian covering the period of 2000–2020, with the total amount of data being 11 years at 1-min cadence. The data set is publicly available (Walker et al., 2022b). It has been demonstrated that large scale average patterns of this data set follow expected behavior. Furthermore, the ability to represent the large scale currents, and their magnetic perturbation on ground is advantageous for interpreting the magnetospheric sources of the changes in the magnetic field on ground. This new data set sets itself apart from empirical models with its temporal nature. Consequently, we have investigated the temporal and spatial variations in the auroral electrojets and the radial magnetic field. We also take advantage of the ability to derive the temporal derivatives by presenting and investigating the time derivative of the radial magnetic field, which has seen little attention in comparison to the horizontal component. The occurrence of stronger time derivatives of the radial magnetic field is shown to have peaks in magnetic latitude, at approximately 67 and 77 magnetic latitude, and the occurrence of a time derivative greater than 25 nT is shown to have peak locations in magnetic local time and magnetic latitude. We suggest that the latitudinal distribution is due to a common latitude of the electrojets or because of the distribution of the magnetometers or due to conductivity effects on coastal magnetometers. We attribute pre midnight peaks in the occurrence of time derivatives greater than 25 nT to the occurrence of substorm onsets and the high latitude peak centered on 9 MLT we suggest is due to PC5 waves, of which our data set is well suited to investigate, or current vortices.

Data Availability Statement

The code for producing Figures 4–6 and Figure 8 is available at Walker et al. (2022a). The data set of divergence-free currents and ground magnetic field perturbations created in this study is publicly available at Walker et al. (2022b). The ground magnetometer data has been retrieved from the SuperMAG collaboration: https://supermag.jhuapl.edu/mag, where data from all stations were downloaded as yearly files, in June 2020 and

has data revision number 5. The solar wind and interplanetary magnetic field measurements has been downloaded from the OMNI database: https://cdaweb.gsfc.nasa.gov/sp_phys/data/omni/hro_1min/. The sunspot number has been retrieved from SILSO: https://www.sidc.be/silso/datafiles.

Acknowledgments
This work was supported by Research Council of Norway under contracts 223252/F50 and 300844/F50 and by the Trond Mohn Foundation. For the ground magnetometer data we thank the institutes who maintain the IMAGE Magnetometer Array: Tromsø Geophysical Observatory of UiT the Arctic University of Norway (Norway), Finnish Meteorological Institute (Finland), Institute of Geophysics Polish Academy of Sciences (Poland), GFZ German Research Centre for Geosciences (Germany), Geological Survey of Sweden (Sweden), Swedish Institute of Space Physics (Sweden), Sodankylä Geophysical Observatory of the University of Oulu (Finland), Polar Geophysical Institute (Russia), and DTU Technical University of Denmark (Denmark). For the processing, baseline removal and distribution of the ground magnetometer data we acknowledge: SuperMAG, PI Jesper W. Gjerloev. For the sunspot number we acknowledge: The World Data Center SILSO, Royal Observatory of Belgium, Brussels. We extend our gratitude to the members of the Understanding Mesoscale Ionospheric Electrodynamics Using Regional Data Assimilation team for the discussions and insight into the topic of study. We also thank the International Space Science Institute in Bern, Switzerland for hosting the team.

References

Aakjær, C. D., Olsen, N., & Finlay, C. C. (2016). Determining polar ionospheric electrojet currents from Swarm satellite constellation magnetic data. *Earth Planets and Space*, *68*(1), 1–14. https://doi.org/10.1186/s40623-016-0509-y

Albertson, V. D., Bozoki, B., Feero, W. E., Kappenman, J. G., Larsen, E. V., Nordell, D. E., et al. (1993). Geomagnetic disturbance effects on power systems. *IEEE Transactions on Power Delivery*, *8*(3), 1206–1216. https://doi.org/10.1109/61.252646

Amm, O. (1997). Ionospheric elementary current systems in spherical coordinates and their application, technical report no. 7 (Vol. *49*). https://doi.org/10.5636/jgg.49.947

Amm, O., & Viljanen, A. (1999). Ionospheric disturbance magnetic field continuation from the ground to the ionosphere using spherical elementary current systems. *Earth Planets and Space*, *51*(6), 431–440. https://doi.org/10.1186/BF03352247

Anderson, B. J., Korth, H., Waters, C. L., Green, D. L., Merkin, V. G., Barnes, R. J., & Dyrud, L. P. (2014). Development of large-scale Birkeland currents determined from the active magnetosphere and planetary electrodynamics response experiment. *Geophysical Research Letters*, *41*(9), 3017–3025. https://doi.org/10.1002/2014GL059941

Birkeland, K. (1908). *The Norwegian aurora polaris expedition, 1902–1903*. H. Aschelhoug. https://doi.org/10.5962/bhl.title.17857

Chapman, S., & Bartels, J. (1940). Geomagnetism, volume II: Analysis of the data, and physical theories.

Chapman, S., & Ferraro, V. C. A. (1931). A new theory of magnetic storms. *Terrestrial Magnetism and Atmospheric Electricity*, *36*(2), 77–97. https://doi.org/10.1029/TE036i002p00077

Cliver, W., & Cliver, E. W. (1994). Solar activity and geomagnetic storms: The first 40 years. *EOS Transactions*, *75*(49), 569–575. https://doi.org/10.1029/94EO02041

Dimmock, A. P., Nykyri, K., Osmane, A., & Pulkkinen, T. I. (2016). Statistical mapping of ULF Pc3 velocity fluctuations in the Earth's dayside magnetosheath as a function of solar wind conditions. *Advances in Space Research*, *58*(2), 196–207. https://doi.org/10.1016/j.asr.2015.09.039

Dimmock, A. P., Rosenqvist, L., Welling, D. T., Viljanen, A., Honkonen, I., Boynton, R. J., & Yordanova, E. (2020). On the regional variability of dB/dt and its significance to GIC. *Space Weather*, *18*(8), e2020SW002497. https://doi.org/10.1029/2020SW002497

Dungey, J. W. (1961). Interplanetary magnetic field and the auroral zones. *Physical Review Letters*, *6*(2), 47–48. https://doi.org/10.1103/PhysRevLett.6.47

Finlay, C. C., Kloss, C., Olsen, N., Hammer, M. D., Tøffner-Clausen, L., Grayver, A., & Kuvshinov, A. (2020). The CHAOS-7 geomagnetic field model and observed changes in the South Atlantic Anomaly. *Earth Planets and Space*, *72*(1), 1–31. https://doi.org/10.1186/s40623-020-01252-9

Frey, H. U., Mende, S. B., Angelopoulos, V., & Donovan, E. F. (2004). Substorm onset observations by IMAGE-FUV. *Journal of Geophysical Research*, *109*(A10), A10304. https://doi.org/10.1029/2004JA010607

Fukushima, N. (1976). Generalized theorem for no ground magnetic effect of vertical currents connected with Pedersen currents in the uniform-conductivity ionosphere. *Report of Ionosphere and Space Research in Japan*, *30*(1–2), 35–40.

Fukushima, N. (1994). Some topics and historical episodes in geomagnetism and aeronomy. *Journal of Geophysical Research*, *99*(A10), 19113. https://doi.org/10.1029/94ja00102

Gjerloev, J. W. (2012). The SuperMAG data processing technique. *Journal of Geophysical Research*, *117*(9), A09213. https://doi.org/10.1029/2012JA017683

Green, D. L., Waters, C. L., Korth, H., Anderson, B. J., Ridley, A. J., & Barnes, R. J. (2007). Technique: Large-scale ionospheric conductance estimated from combined satellite and ground-based electromagnetic data. *Journal of Geophysical Research*, *112*(5), e2022JA030573. https://doi.org/10.1029/2006JA012069

Haaland, S. E., Paschmann, G., Förster, M., Quinn, J. M., Torbert, R. B., McIlwain, C. E., et al. (2007). High-latitude plasma convection from Cluster EDI measurements: Method and IMF-dependence. *Annales Geophysicae*, *25*(1), 239–253. https://doi.org/10.5194/angeo-25-239-2007

Harang, L. (1946). The mean field of disturbance of polar geomagnetic storms. *Journal of Geophysical Research*, *51*(3), 353. https://doi.org/10.1029/te051i003p00353

Hynönen, R., Tanskanen, E. I., & Francia, P. (2020). Solar cycle evolution of ULF wave power in solar wind and on ground. *Journal of Space Weather and Space Climate*, *10*, 43. https://doi.org/10.1051/swsc/2020046

Juusola, L., Amm, O., & Viljanen, A. (2006). One-dimensional spherical elementary current systems and their use for determining ionospheric currents from satellite measurements. *Earth Planets and Space*, *58*(5), 667–678. https://doi.org/10.1186/BF03351964

Juusola, L., Kauristie, K., Vanhamäki, H., Aikio, A., & van de Kamp, M. (2016). Comparison of auroral ionospheric and field-aligned currents derived from Swarm and ground magnetic field measurements. *Journal of Geophysical Research A: Space Physics*, *121*(9), 9256–9283. https://doi.org/10.1002/2016JA022961

Juusola, L., Vanhamäki, H., Viljanen, A., & Smirnov, M. (2020). Induced currents due to 3D ground conductivity play a major role in the interpretation of geomagnetic variations. *Annales Geophysicae*, *38*(5), 983–998. https://doi.org/10.5194/angeo-38-983-2020

King, J. H., & Papitashvili, N. E. (2005). Solar wind spatial scales in and comparisons of hourly Wind and ACE plasma and magnetic field data. *Journal of Geophysical Research*, *110*(A2), A02104. https://doi.org/10.1029/2004JA010649

Koskinen, H. E. J., & Pulkkinen, T. I. (1995). Midnight velocity shear zone and the concept of Harang discontinuity. *Journal of Geophysical Research*, *100*(A6), 9539. https://doi.org/10.1029/95ja00228

Laundal, K. M., Finlay, C. C., Olsen, N., & Reistad, J. P. (2018). Solar wind and seasonal influence on ionospheric currents from Swarm and CHAMP measurements. *Journal of Geophysical Research: Space Physics*, *123*(5), 4402–4429. https://doi.org/10.1029/2018JA025387

Laundal, K. M., Gjerloev, J. W., Østgaard, N., Reistad, J. P., Haaland, S., Snekvik, K., et al. (2016). The impact of sunlight on high-latitude equivalent currents. *Journal of Geophysical Research A: Space Physics*, *121*(3), 2715–2726. https://doi.org/10.1002/2015JA022236

Laundal, K. M., Reistad, J. P., Hatch, S. M., Madelaire, M., Walker, S. J., Hovland, A. Ø., et al. (2022). Local mapping of polar ionospheric electrodynamics. *Journal of Geophysical Research: Space Physics*, *127*(5), e2022JA030356. https://doi.org/10.1029/2022JA030356

Laundal, K. M., & Toresen, M. (2018). klaundal/pyAMPS: pyAMPS 0.1.0. https://doi.org/10.5281/ZENODO.1182931

Laundal, K. M., Yee, J.-H. H., Merkin, V. G., Gjerloev, J. W., Vanhamäki, H., Reistad, J. P., et al. (2021). Electrojet estimates from mesospheric magnetic field measurements. *Journal of Geophysical Research: Space Physics*, *126*(5), 1–17. https://doi.org/10.1029/2020ja028644

Madelaire, M., Laundal, K. M., Reistad, J. P., Hatch, S. M., & Ohma, A. (2022). Transient high latitude geomagnetic response to rapid increases in solar wind dynamic pressure. *Frontiers in Astronomy and Space Sciences*, *9*, 188. https://doi.org/10.3389/FSPAS.2022.953954/BIBTEX

Marsal, S., Torta, J. M., Segarra, A., & Araki, T. (2017). Use of spherical elementary currents to map the polar current systems associated with the geomagnetic sudden commencements on 2013 and 2015 St. Patrick's Day storms. *Journal of Geophysical Research: Space Physics*, *122*(1), 194–211. https://doi.org/10.1002/2016JA023166

Molinski, T. S. (2002). Why utilities respect geomagnetically induced currents. *Journal of Atmospheric and Solar-Terrestrial Physics*, *64*(16), 1765–1778. https://doi.org/10.1016/S1364-6826(02)00126-8

Newell, P. T., Liou, K., Gjerloev, J. W., Sotirelis, T., Wing, S., & Mitchell, E. J. (2016). Substorm probabilities are best predicted from solar wind speed. *Journal of Atmospheric and Solar-Terrestrial Physics*, *146*, 28–37. https://doi.org/10.1016/j.jastp.2016.04.019

Nosé, M., Iyemori, T., Sugiura, M., & Slavin, J. A. (1995). A strong dawn/dusk asymmetry in Pc5 pulsation occurrence observed by the DE-1 satellite. *Geophysical Research Letters*, *22*(15), 2053–2056. https://doi.org/10.1029/95GL01794

Nykyri, K., Ma, X., Dimmock, A., Foullon, C., Otto, A., & Osmane, A. (2017). Influence of velocity fluctuations on the Kelvin-Helmholtz instability and its associated mass transport. *Journal of Geophysical Research: Space Physics*, *122*(9), 9489–9512. https://doi.org/10.1002/2017JA024374

Oliveira, D. M., & Ngwira, C. M. (2017). Geomagnetically induced currents: Principles. *Brazilian Journal of Physics*, *47*(5), 552–560. https://doi.org/10.1007/s13538-017-0523-y

Olsen, N. (1996). A new tool for determining ionospheric currents from magnetic satellite data. *Geophysical Research Letters*, *23*(24), 3635–3638. https://doi.org/10.1029/96GL02896

Plaschke, F., Hietala, H., Archer, M., Blanco-Cano, X., Kajdič, P., Karlsson, T., et al. (2018). *Jets downstream of collisionless shocks* (Vol. 214). Springer Netherlands. https://doi.org/10.1007/s11214-018-0516-3

Pulkkinen, A., Amm, O., & Viljanen, A. (2003). Separation of the geomagnetic variation field on the ground into external and internal parts using the spherical elementary current system method. *Earth Planets and Space*, *55*(3), 117–129. https://doi.org/10.1186/BF03351739

Pulkkinen, A., Amm, O., Viljanen, A., Korja, T., Hjelt, S. E., Kaikkonen, P., & Tregubenko, V. (2003). Ionospheric equivalent current distributions determined with the method of spherical elementary current systems. *Journal of Geophysical Research*, *108*(A2), 1053. https://doi.org/10.1029/2001JA005085

Richmond, A. (1995). Ionospheric electrodynamics. In H. Volland (Ed.), *Handbook of atmospheric electrodynamics* (Vol. 1, pp. 249–290). CRC Press. https://doi.org/10.1201/9780203713297

Rogers, N. C., Wild, J. A., Eastoe, E. F., Gjerloev, J. W., & Thomson, A. W. (2020). A global climatological model of extreme geomagnetic field fluctuations. *Journal of Space Weather and Space Climate*, *10*, 5. https://doi.org/10.1051/SWSC/2020008

Ronchi, C., Iacono, R., & Paolucci, P. S. (1996). The "Cubed sphere": A new method for the solution of partial differential equations in spherical geometry. *Journal of Computational Physics*, *124*(1), 93–114. https://doi.org/10.1006/jcph.1996.0047

Sadourny, R. (1972). Conservative finite-difference approximations of the primitive equations on quasi-uniform spherical grids. *Monthly Weather Review*, *100*(2), 136–144. https://doi.org/10.1175/1520-0493(1972)100⟨0136:CFAOTP⟩2.3.CO;2

Schillings, A., Palin, L., Opgenoorth, H. J., Hamrin, M., Rosenqvist, L., Gjerloev, J. W., et al. (2022). Distribution and occurrence frequency of dB/dt spikes during magnetic storms 1980–2020. *Space Weather*, *20*(5), e2021SW002953. https://doi.org/10.1029/2021SW002953

Schove, D. J. (1983). Sunspot cycles.

Siscoe, G. L. (2001). 70 years of magnetospheric modeling. In *Geophysical monograph series* (Vol. 125, pp. 211–227). American Geophysical Union (AGU). https://doi.org/10.1029/GM125p0211

Tanskanen, E. I., Slavin, J. A., Tanskanen, A. J., Viljanen, A., Pulkkinen, T. I., Koskinen, H. E., & Eastwood, J. (2005). Magnetospheric substorms are strongly modulated by interplanetary high-speed streams. *Geophysical Research Letters*, *32*(16), 1–4. https://doi.org/10.1029/2005GL023318

Tanskanen, E. I., Viljanen, A., Pulkkinen, T. I., Pirjola, R., Häkkinen, L., Pulkkinen, A., & Amm, O. (2001). At substorm onset, 40% of AL comes from underground. *Journal of Geophysical Research*, *106*(A7), 13119–13134. https://doi.org/10.1029/2000ja900135

Vanhamäki, H., Amm, O., & Viljanen, A. (2003). One-dimensional upward continuation of the ground magnetic field disturbance using spherical elementary current systems. *Earth Planets and Space*, *55*(10), 613–625. https://doi.org/10.1186/BF03352468

Vanhamäki, H., & Juusola, L. (2020). Introduction to spherical elementary current systems. In *Ionospheric multi-spacecraft analysis tools* (pp. 5–33). Springer International Publishing. https://doi.org/10.1007/978-3-030-26732-2{_}2

Vanhamäki, H., Viljanen, A., Pirjola, R., & Amm, O. (2013). Deriving the geomagnetically induced electric field at the Earth's surface from the time derivative of the vertical magnetic field. *Earth Planets and Space*, *65*(9), 997–1006. https://doi.org/10.5047/eps.2013.03.013

Viljanen, A., Nevanlinna, H., Pajunpää, K., & Pulkkinen, A. (2001). Time derivative of the horizontal geomagnetic field as an activity indicator. *Annales Geophysicae*, *19*(9), 1107–1118. https://doi.org/10.5194/angeo-19-1107-2001

Walker, S. J., Laundal, K. M., Reistad, J. P., Hatch, S. M., & Ohma, A. (2022a). 08walkersj/SECpy_Plotting: SECpy_Plotting 0.1.0. https://doi.org/10.5281/zenodo.7138948

Walker, S. J., Laundal, K. M., Reistad, J. P., Hatch, S. M., & Ohma, A. (2022b). Statistics of temporal variations in the auroral electrojets over Fennoscandia [Dataset]. Zenodo. http://www.doi.org/10.5281/zenodo.6505230

Weigel, R. S., Klimas, A. J., & Vassiliadis, D. (2003). Solar wind coupling to and predictability of ground magnetic fields and their time derivatives. *Journal of Geophysical Research*, *108*(A7), 1298. https://doi.org/10.1029/2002JA009627

Weygand, J. M., Amm, O., Angelopoulos, V., Milan, S. E., Grocott, A., Gleisner, H., & Stolle, C. (2012). Comparison between SuperDARN flow vectors and equivalent ionospheric currents from ground magnetometer arrays. *Journal of Geophysical Research*, *117*(5), 5325. https://doi.org/10.1029/2011JA017407

Weygand, J. M., Amm, O., Viljanen, A., Angelopoulos, V., Murr, D., Engebretson, M. J., et al. (2011). Application and validation of the spherical elementary currents systems technique for deriving ionospheric equivalent currents with the North American and Greenland ground magnetometer arrays. *Journal of Geophysical Research*, *116*(3), A03305. https://doi.org/10.1029/2010JA016177

Weygand, J. M., Engebretson, M. J., Pilipenko, V. A., Steinmetz, E. S., Moldwin, M. B., Connors, M. G., et al. (2021). SECS analysis of nighttime magnetic perturbation events observed in Arctic Canada. *Journal of Geophysical Research: Space Physics*, *126*(11), e2021JA029839. https://doi.org/10.1029/2021JA029839

Weygand, J. M., McPherron, R. L., Frey, H. U., Amm, O., Kauristie, K., Viljanen, A., & Koistinen, A. (2008). Relation of substorm onset to Harang discontinuity. *Journal of Geophysical Research*, *113*(4), A04213. https://doi.org/10.1029/2007JA012537

Weygand, J. M., & Wing, S. (2016). Comparison of DMSP and SECS region-1 and region-2 ionospheric current boundary. *Journal of Atmospheric and Solar-Terrestrial Physics*, *143–144*, 8–13. https://doi.org/10.1016/j.jastp.2016.03.002

Yee, J. H., Gjerloev, J., & Wu, D. (2021). Remote sensing of magnetic fields induced by electrojets from space: Measurement techniques and sensor design. In *Space physics and aeronomy, upper atmosphere dynamics and energetics* (pp. 451–468). Wiley. https://doi.org/10.1002/9781119815631.ch21

Zmuda, A. J., Martin, J. H., & Heuring, F. T. (1966). Transverse magnetic disturbances at 1100 kilometers in the auroral region. *Journal of Geophysical Research*, *71*(21), 5033–5045. https://doi.org/10.1029/jz071i021p05033